nature physics

Article

https://doi.org/10.1038/s41567-024-02759-8

An electronic microemulsion phase emerging from a quantum crystal-to-liquid transition

Received: 19 February 2024

Accepted: 6 December 2024

Published online: 20 January 2025

Check for updates

Jiho Sung[1,2,12], Jue Wang[1,2,12], Ilya Esterlis[2,3,12], Pavel A. Volkov[2,4,12], Giovanni Scuri[1,2,5], You Zhou[6], Elise Brutschea[1], Takashi Taniguchi[7], Kenji Watanabe[7], Yubo Yang[8], Miguel A. Morales[8], Shiwei Zhang[8], Andrew J. Millis[8,9], Mikhail D. Lukin[2], Philip Kim[2,10], Eugene Demler[11] ✉ & Hongkun Park[1,2] ✉

Strongly interacting electronic systems often exhibit a complicated phase diagram that results from the competition between different quantum ground states. One feature of these phase diagrams is the emergence of microemulsion phases, where regions of different phases self-organize across multiple length scales. The experimental characterization of these microemulsions can pose considerable challenges, as the long-range Coulomb interaction microscopically mingles with the competing states. Here we observe the signatures of the microemulsion between an electronic Wigner crystal and an electron liquid in a $MoSe_2$ monolayer using cryogenic reflectance and magneto-optical spectroscopy. We find that the transition into this microemulsion state is marked by anomalies in exciton reflectance, spin susceptibility and umklapp scattering, establishing it as a distinct phase of electronic matter.

The interplay between Coulomb interactions and kinetic energy is at the heart of correlated electron physics and underlies the emergence of many exotic phases of matter. Despite a plethora of complex phenomena, such systems share general principles. Of particular importance is the fact that long-range Coulomb forces forbid direct first-order phase transitions, which are instead replaced by intermediate phases with intricate mesoscale or nanoscale structures[1–7]. Such ideas have been proposed to explain the phase diagrams of strongly correlated materials, including high transition temperature superconductors[8], colossal magnetoresistance manganates[9,10] and the excitonic Wigner crystal-to-superfluid phase transition in semiconductors[11,12]. However, a direct confirmation of electronic mixed phases is lacking in solid-state systems because crystalline lattice transformations often coincide with electronic phase transitions[9,10]. Theoretical and experimental characterization of mixture phases remains challenging due to the multiscale nature of the electronic order.

Here we focus on the case of the density-driven crystal-to-liquid transition in a low-density two-dimensional electron gas (2DEG) hosted in an atomically thin semiconductor. The low electron densities in these systems ensure that electronic transitions do not trigger lattice instabilities, making it a model correlated electron system with negligible lattice effects. In the low-density regime, quantum Monte Carlo (QMC) studies predict that electrons spontaneously arrange into a crystalline solid—the Wigner crystal—when the ratio of the Coulomb interaction to the kinetic energy, $r_s(=m_e^* e^2/\left(4\pi\varepsilon_0\varepsilon\hbar^2\sqrt{\pi n}\right))$, is around 30 (refs. 13,14). Here, m_e^*, e, ε_0, ε, $\hbar$ and n denote the effective mass of electrons, elementary charge, vacuum permittivity, dielectric

[1]Department of Chemistry and Chemical Biology, Harvard University, Cambridge, MA, USA. [2]Department of Physics, Harvard University, Cambridge, MA, USA. [3]Department of Physics, University of Wisconsin-Madison, Madison, WI, USA. [4]Department of Physics, University of Connecticut, Storrs, CT, USA. [5]E. L. Ginzton Laboratory, Stanford University, Stanford, CA, USA. [6]Department of Materials Science and Engineering, University of Maryland, College Park, MD, USA. [7]National Institute for Materials Science, Tsukuba, Japan. [8]Center for Computational Quantum Physics, Flatiron Institute, New York, NY, USA. [9]Department of Physics, Columbia University, New York, NY, USA. [10]John A. Paulson School of Engineering and Applied Sciences, Harvard University, Cambridge, MA, USA. [11]Institute for Theoretical Physics, ETH Zürich, Zürich, Switzerland. [12]These authors contributed equally: Jiho Sung, Jue Wang, Ilya Esterlis, Pavel A. Volkov. ✉e-mail: demlere@phys.ethz.ch; hpark@g.harvard.edu

https://doi.org/10.1038/s41567-024-02759-8

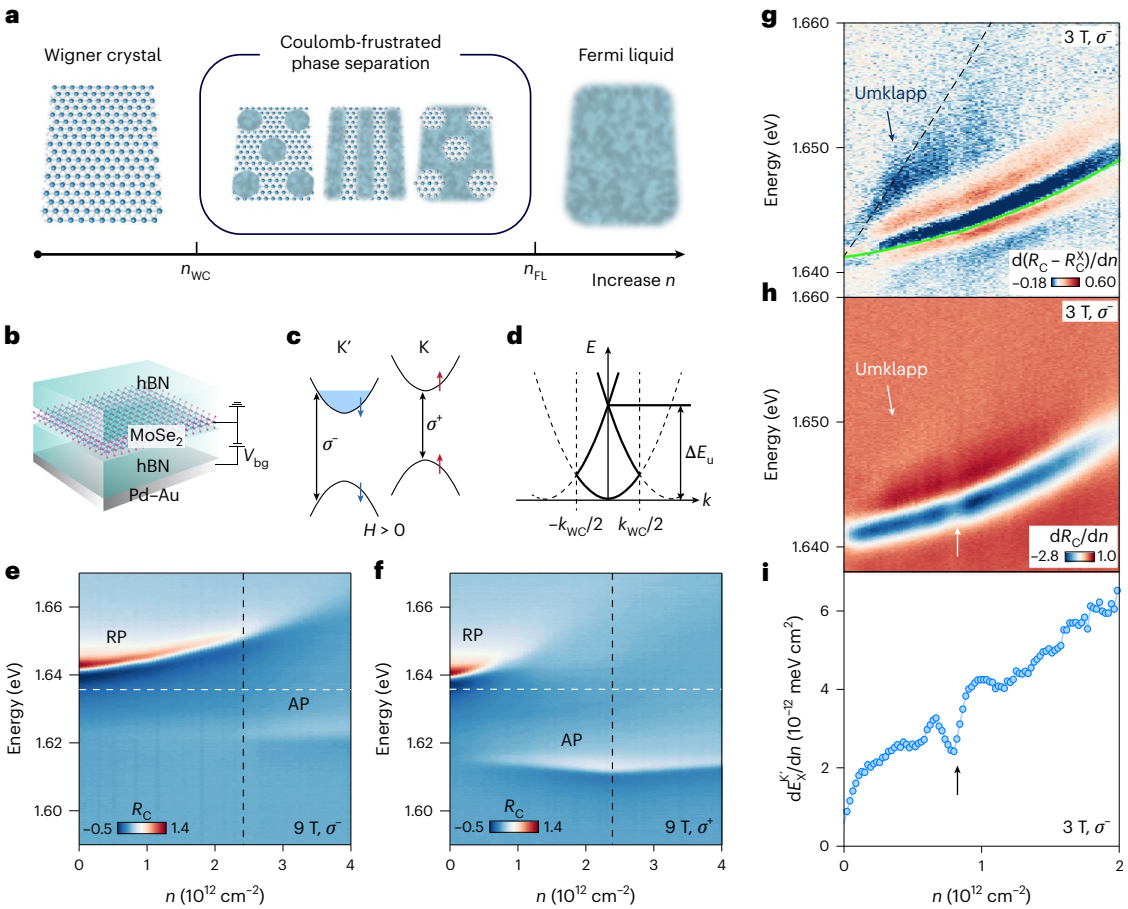

Fig. 1 | Two-dimensional electron phases and exciton spectroscopy. **a**, Schematic phase diagram of a 2D electron system including a Wigner crystal, a Fermi liquid and the intermediate phases composed of mesoscale or nanoscale regions containing the two competing phases resulting from Coulomb-frustrated phase separation. **b**, Schematic of the device structure. A $MoSe_2$ monolayer is encapsulated by hBN and grounded. A bottom gate voltage, V_{bg}, is applied to the Pd–Au back gate to control the electron density in a $MoSe_2$ monolayer. **c**, Schematic showing the relative energy alignment of the electronic band extrema at the K and K′ valleys under a positive magnetic field. It also shows the spin–valley locking and the valley optical section rule. **d**, Schematic of the exciton dispersion showing the higher-energy resonance at exciton momentum $k = 0$, arising from umklapp scattering by the periodic potential of the electron Wigner crystal. The energy splitting ΔE_u from the main exciton resonance is determined by reciprocal Wigner crystal lattice vector k_{WC}. **e**,**f**, Left (σ^-) (**e**) and right (σ^+) (**f**) circularly polarized reflectance contrast spectra at 9 T and at a base lattice temperature of 16 mK as a function of electron density under light power of 0.7 nW. Black dashed lines show the density (2.35×10^{12} cm^{-2}) above which electrons start to fill the second valley (K) of opposite spin. White dashed lines mark the energy (1.636 eV) for obtaining the magneto-optical signal, $\tilde{M}$. **g**, Colour map of the derivative of reflectance contrast spectra (3 T, σ^-) with respect to electron density. A Lorentz fitted exciton peak was subtracted to emphasize the higher-energy features from umklapp scattering. Line profile of the reflectance contrast spectra (3 T, σ^-), the dispersive Lorentzian fit and their subtraction at $n = 0.35 \times 10^{12}$ cm^{-2} are shown in Supplementary Fig. 10. The green line represents the fitted exciton resonance energy and the black dashed line indicates the expected resonance energy from umklapp scattering of excitons. The difference between the two resonances correspond to the energy splitting ΔE_u. **h**, Colour map of the derivative of reflectance contrast spectra (3 T, σ^-) with respect to electron density, without subtracting the fitted exciton Lorentzian. Note the clear anomaly near 0.82×10^{12} cm^{-2} and the higher-energy umklapp feature. **i**, Derivative of fitted exciton or RP resonance energy with respect to electron density shows a discontinuity around 0.82×10^{12} cm^{-2}. Reflectance contrast spectra measurements in panels **g**–**i** were performed under light power of 70 pW at a base lattice temperature of 16 mK. We used exciton or RP Zeeman energy splitting to estimate the electron temperature under this condition (Supplementary Section 8).

constant, reduced Planck constant and electron density, respectively. With increasing electron density, this Wigner crystal melts into a liquid owing to increasing quantum fluctuations. It is predicted that this quantum melting proceeds by means of a sequence of intermediate microemulsion phases[1–3,7] (Fig. 1a).

Previous studies of the transition from the liquid phase at higher densities to the crystalline phase at lower densities primarily relied on transport measurements[15–20]. Recently, transport signatures of unconventional magnetic behaviour have been reported close to the metal–insulator transition[20]. However, such measurements do not allow the identification of intermediate microemulsion phases because the signatures of microemulsion phases in transport are extremely difficult to predict theoretically[21]. Moreover, thermodynamic probes that can identify different electronic phases and transitions between them are more desirable to disentangle the electron correlation effect from a disorder-induced effect.

Electron Wigner crystal in a $MoSe_2$ monolayer

The recent discovery of Wigner crystal phases in atomically thin transition metal dichalcogenides presents an avenue to investigate the fundamental questions regarding exotic phases of matter near the quantum crystal-to-liquid transition[22,23]. In these materials, optically generated excitons are sensitive to both charge and spin order of the surrounding electrons[22–25], and thus they provide a local detection scheme that gives insights into the electronic phase diagram.

In our experiment, we used dilution refrigerator-based scanning confocal microscopy to probe the melting of an electron Wigner crystal formed in a $MoSe_2$ monolayer encapsulated by hexagonal boron nitride (hBN) (device D1 in Fig. 1b; see also Extended Data Fig. 1). We conducted measurements of circular polarization resolved spectroscopy as a function of electron density (tuned by a gate voltage), perpendicular magnetic field and temperature (Methods). In a $MoSe_2$ monolayer, the lowest energy optical transitions occur in the K (K′) valleys. In these transitions, right (σ^+) and left (σ^-) circularly polarized light selectively couples to up (down) spin electrons owing to the optical selection rules and spin–valley locking[25] (Fig. 1c). The exciton–electron interaction depends on whether a K (K′) valley exciton interacts with a K′ (K) valley electron (case 1) or a K (K′) valley electron (case 2). In case 1, the interaction is strong, leading to the emergence of higher-energy repulsive polaron (RP) and lower-energy attractive polaron (AP) branches in the spectrum[26]. In case 2, the interaction, stemming from an exchange interaction and Pauli blocking[25,26], is comparatively weaker. The difference between intravalley and intervalley exciton–electron interaction enables the detection of electron spin polarization by circularly polarized light.

Figure 1e,f shows representative reflectance contrast spectra R_C (defined in Methods) at $B = 9$ T with σ^+ and σ^- light as a function of electron density. A perpendicular magnetic field lifts the degeneracy of the band minima, so the electrons doping the $MoSe_2$ monolayer are spin and valley polarized at low electron doping (in this case, with spin down in the K′ valley, as shown in Fig. 1c). The σ^+-reflectance contrast spectrum that probes the K valley (Fig. 1f) shows two polaron branches due to intervalley exciton–electron interaction, whereas the σ^- spectrum probing the K′ valley does not (Fig. 1e). At higher doping densities ($n > 2.35 \times 10^{12}$ cm^{-2}), the electron starts to fill both valleys, and two polaron branches are present in both spectra. The inequivalence between σ^+ and σ^- spectra reveals that the system is still partially spin polarized.

The density dependence of the exciton reflectance reveals two important features. The optical response is not a smooth function of the electron density. Instead, it is segmented by anomalies, the most prominent of which occurs near $n_* = 0.82 \times 10^{12}$ cm^{-2} (upward arrows in Fig. 1h,i). Because the excitonic properties are sensitive to the charge and spin properties of the surrounding electrons, these anomalies are indications of a change in the electronic state. The detection of this previously unobserved feature is facilitated by a base lattice temperature of 16 mK inside our dilution refrigerator (the electron temperature is higher owing to light absorption, as discussed below) and a low excitation light power below 0.7 nW (Methods).

At electron densities below $n_{WC} = 0.35 \times 10^{12}$ cm^{-2}, we observed a higher-energy spectral feature (Fig. 1g) that blueshifts linearly with electron density (along the black dashed line in Fig. 1g)[22]. This higher-energy resonance originates from the umklapp scattering of excitons by the periodic potential created by the electron Wigner crystal: the exciton state with momentum $k = k_{WC}$ (k_{WC} denotes the reciprocal lattice vector of the electron Wigner crystal) is folded back to the zero-momentum light cone and acquires a finite oscillator strength[22] (Fig. 1d). Notably, at densities greater than n_{WC} the feature changes slope and extends to much higher densities than previously observed, albeit with a pronounced broadening. At sufficiently high electron densities (Fig. 1g,h) the feature vanishes. Similar umklapp features are observed in other spots in D1 and in another $MoSe_2$ monolayer device, D2 (Extended Data Fig. 2).

Taken together, the spectral anomalies and the extended umklapp feature demonstrate an unexpected evolution of the electronic state between a simple Wigner crystal and liquid phases. Before investigating the behaviour in this intermediate density range, we first established that the magnetic properties of the system at sufficiently high and low electron densities are those of a Fermi liquid and Wigner crystal, respectively.

Fermi liquid and Wigner crystal

The magnetic response of a Fermi liquid can be characterized by the critical density for full spin polarization at non-zero magnetic fields and the spin susceptibility near zero field. As discussed in the preceding section, the filling of electrons into the K valley results in the intervalley polaronic dressing of K′-valley excitons, and vice versa. We can therefore use the onset of the σ^- AP resonance in the reflectance spectra (Fig. 1e,f) to determine the critical density at which the fully spin-polarized liquid starts to become partially polarized[25] (Supplementary Section 1).

Figure 2a shows the critical densities determined by the onset of the σ^- AP resonance at various magnetic fields. For a given magnetic field, we find that the system is fully spin polarized below a critical electron density, as expected for a Fermi liquid[27]. The critical densities extracted from our experiments are in good agreement with predictions from a fixed-node diffusion QMC model[14,27] for a clean 2DEG (Fig. 2a). We note that the critical density we observe is an order of magnitude higher than that predicted for non-interacting electrons in $MoSe_2$ (ref. 25), which demonstrates the strong Coulomb interactions present in our system (Supplementary Section 2).

To extract the spin susceptibility of the 2DEG at low magnetic fields we obtained the magneto-optical signal $\tilde{M} = \left(I^{\sigma^+}/I^{\sigma^+}_{max} - I^{\sigma^-}/I^{\sigma^-}_{max}\right)/\left(I^{\sigma^+}/I^{\sigma^+}_{max} + I^{\sigma^-}/I^{\sigma^-}_{max}\right)$, which is the difference in normalized reflected intensity between $\sigma^\pm$ light divided by their sum. Here, $I(I_{max})$ denotes the reflected intensity at a density of 1.0×10^{13} cm^{-2}. We computed $\tilde{M}$ using reflectance spectra in a narrow energy range, 5 meV red-detuned from the main exciton resonance at zero doping. Optical selection rules imply that $\tilde{M}$ is proportional to the imbalance of electrons in the lowest conduction bands (Fig. 1c), which, owing to spin–valley locking, can be interpreted as the spin (or valley) polarization of the electrons[24,28] (Supplementary Section 3). The field dependence of $\tilde{M}(H)$, where H is the applied magnetic field, further allowed us to extract the spin susceptibility χ of electrons shown in Fig. 2b, which is normalized to the spin susceptibility of the non-interacting 2DEG, $\chi_0 = \left(\frac{g\mu_B}{2}\right)^2 \frac{m^*}{\pi\hbar^2}$, where g is the g factor for the conduction band and μ_B denotes the Bohr magneton[29]. (See Supplementary Section 4 for other methods to obtain the spin susceptibility, that yield similar results). As anticipated, χ/χ_0 grows with decreasing electron density because the Coulomb interaction favours spin polarization.

Similar to the critical field for full polarization, this experimentally extracted spin susceptibility agrees well with predictions from QMC studies[14,27] (dashed line in Fig. 2b), further confirming that the high-density electron system is well described as a clean, strongly interacting two-dimensional Fermi liquid. A Fermi liquid should, furthermore, exhibit a temperature-independent spin susceptibility[30] for $T \ll E_F$, where E_F is the (renormalized) Fermi energy. As described below, we indeed observed a temperature-independent susceptibility above a certain density denoted by n_{FL} (Fig. 3d).

The magnetic response of the low-density ($n < n_{WC}$) Wigner crystal is drastically different from that of a Fermi liquid. In the Wigner crystal phase, the electrons are localized in real space so that the spins are correlated only by the (extremely weak) exchange interaction[31,32]. For temperatures above the exchange interaction scale but below the melting temperature of the Wigner crystal, the magnetic behaviour should thus be that of independent spins, with magnetization following the Brillouin function $M = \frac{1}{2} g\mu_B n \tanh\left(\frac{g\mu_B H}{2k_B T_{elec}}\right)$, where k_B is the Boltzmann constant, and an associated Curie susceptibility $\chi = \left(\frac{g\mu_B}{2}\right)^2 \frac{n}{k_B T}$ (refs. 2,7). In sharp contrast to the liquid phase, the susceptibility is expected to increase with electron density and depend strongly on temperature.

To probe the magnetism of the low-density regime, where light-induced heating becomes important, we used a continuous-wave

https://doi.org/10.1038/s41567-024-02759-8

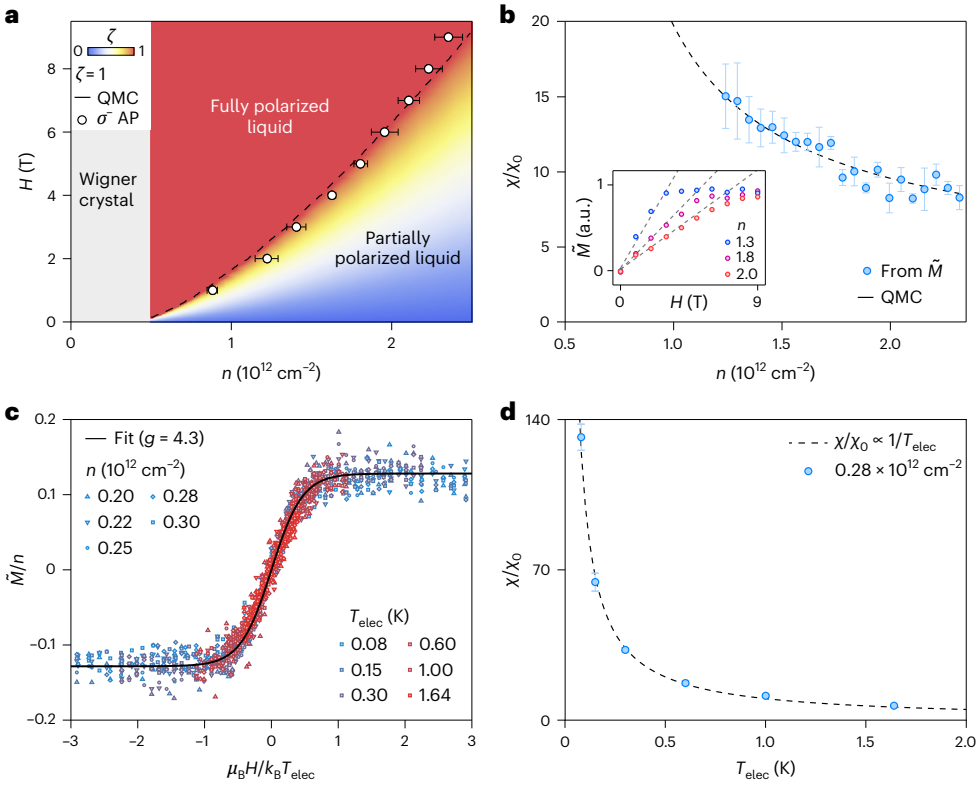

Fig. 2 | Fermi-liquid and Wigner-crystal magnetism. a, Spin polarization of the 2D electron system with respect to electron density and magnetic field. The colour scale represents the spin polarization ζ of a 2D Fermi liquid and the dashed curve is the boundary of the fully polarized liquid, both obtained from QMC simulations. We used the conduction band g factor of 4.3, the dielectric constant $\varepsilon = 4.6$ and the effective mass of electrons $m_e^* = 0.7m_0$ as parameters for the QMC simulations, where m_0 is the bare electron mass. We determine the onset densities of σ^- AP at each magnetic field (empty dots) using a linear fit, with error bars indicating one standard error. **b**, Reduced spin susceptibility as a function of electron density obtained from QMC (dashed curve) and computed $\tilde{M}$ from the reflectance contrast spectra (blue dots). The error bars represent one standard error of the linear fit to the low-field slope of the computed $\tilde{M}$. We conducted QMC simulations with the same values of the g factor and effective mass as in **a** and used the dielectric constant as a free parameter. A good fit was obtained by using the dielectric constant $\varepsilon = 4$, which deviates by about 10% from the value used in **a**. Inset: $\tilde{M}$ as a function of magnetic field for an electron density of 1.3, 1.8 and 2.0×10^{12} cm^{-2}. **c**, Scaled magnetization curves ($\tilde{M}/n$ as a function of $\mu_B H/k_B T$) in the Wigner crystal regime. The shapes and colours of the markers represent different electron densities and temperatures. The black curve is a fit by Brillouin function with $g = 4.3$. **d**, Reduced spin susceptibility (χ/χ_0) at $n = 0.28 \times 10^{12}$ cm^{-2} as a function of electron temperature, showing Curie susceptibility.

laser at a single energy (1.636 eV, white dashed lines in Fig. 1e,f) below the exciton resonance to obtain $\tilde{M}$ as a function of electron density and magnetic field (Methods): this approach reduced the light power reaching the sample. By fitting the measured $\tilde{M}(n, H)$ at different temperatures using the Brillouin function, we determined the conduction band g factor and the electron temperature (T_{elec}). With a 60 fW diffraction-limited laser spot, we reached an electronic temperature of 80 mK with the device at a base lattice temperature of 16 mK (Extended Data Fig. 3). When the temperature exceeded 150 mK, the extracted electron temperatures agreed with the lattice temperatures (Supplementary Section 5).

Figure 2c shows a plot of $\tilde{M}$ normalized by the electron density ($\tilde{M}/n$) as a function of magnetic field normalized by the electron temperature ($\mu_B H/k_B T_{elec}$) in the Wigner crystal regime ($n < n_{WC} = 0.35 \times 10^{12}$ cm^{-2}). As clearly seen in the figure, the data at different electron densities and electron temperatures collapse onto a single curve. When we extracted the spin susceptibility at various temperatures from linear fits to $\tilde{M}(H)$ at small fields, we found an inverse relationship between the spin susceptibility and electron temperature (Fig. 2d). The successful application of the scaling analysis across different electron densities and temperatures demonstrates that the behaviour of the electrons in the low-density regime ($n < n_{WC}$) is well described by a Wigner crystal with an independent spin localized at each lattice site.

Crystal–liquid coexistence in microemulsion phase

Following the demonstration of a conventional Fermi liquid at high density and a Wigner crystal at low density, we proceed to characterize charge and spin properties of the intermediate density range in our $MoSe_2$ system. We begin with a detailed analysis of the exciton umklapp scattering (Fig. 1d,g,h). To further enhance the relevant features, we subtracted the fitted main exciton spectral profile from the reflectance contrast, took the derivative with respect to the electron density and plotted it against the energy detuning from main exciton peak (Fig. 3a). We then determined the energy splitting between the umklapp feature and the main exciton peak as well as the umklapp linewidth, as shown in Fig. 3b,c (See also Supplementary Section 6).

When $n_{WC} < 0.35 \times 10^{12}$ cm^{-2}, the umklapp linewidth was close to the main exciton linewidth, whereas the energy splitting increased linearly with the electron density $\Delta E_u = \frac{h^2 n}{\sqrt{3} m_X}$, confirming that all electrons are crystallized into a triangular lattice Wigner crystal[22]. However, when $n > n_{WC}$, ΔE_u became only weakly dependent on density, which suggests that the periodicity of the underlying electron lattice is approximately independent of n. As the electron density approached n_*, the density at which the exciton intensity anomaly is observed in Fig. 1h,i (see also Extended Data Fig. 4), the width of the umklapp feature increased rapidly (Fig. 3c (middle)). This broadening arises from the

https://doi.org/10.1038/s41567-024-02759-8

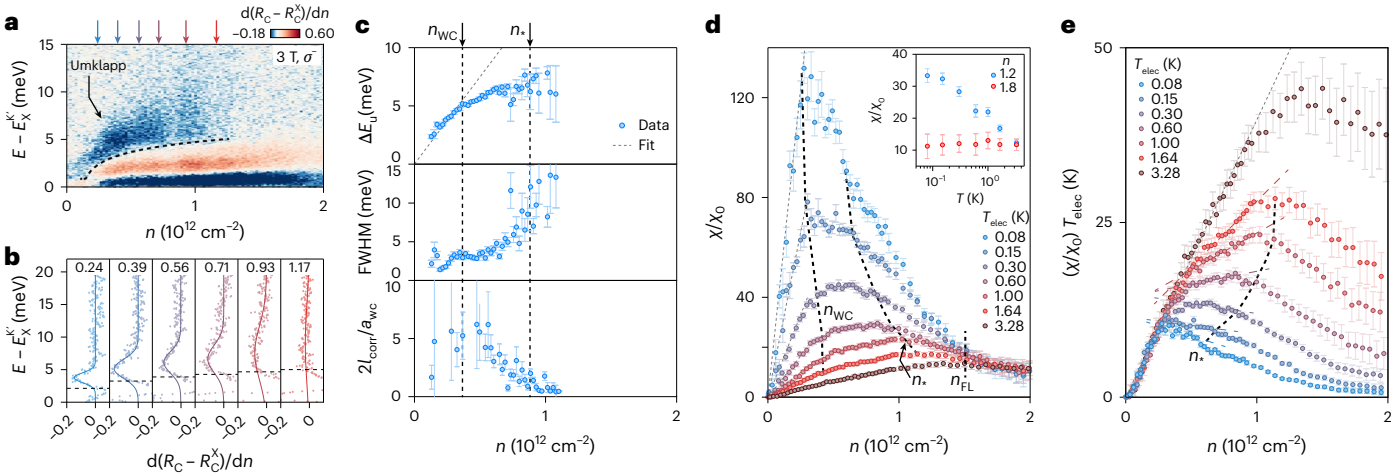

Fig. 3 | Quantum melting of a Wigner crystal. a, Colour map of the derivative of reflectance contrast spectra (3 T, σ^-), plotted against electron density and the energy detuning from the main exciton resonance. A Lorentzian-fitted exciton peak was subtracted to emphasize the higher-energy feature from umklapp scattering. **b**, Cross-sections through the 2D map indicated by coloured arrows in **a** at a fixed electron density, denoted by numbers in units of 10^{12} cm^{-2}. Each spectrum is fitted with a Gaussian function, represented by coloured solid lines. Black dashed lines in **a** and **b** mark the energy above that which we used for fitting to avoid contributions from the residual exciton peak after subtraction. **c**, Energy difference between exciton and umklapp features as a function of electron density (top). The grey dashed line is a linear fit assuming that all the electrons are crystallized into a triangular lattice which provides the umklapp scattering momentum for excitons. From the slope $\Delta E_u/n = h^2/\sqrt{3}m_X$, we extracted the exciton mass, $m_X = (1.15 \pm 0.05)m_0$. The full-width at half-maximum (FWHM) of umklapp scattering as a function of electron density (middle). The estimated crystalline correlation length as a function of electron density (bottom). The black arrows on the top x axis and black dashed lines indicate the characteristic densities, n_{WC} and n_*. The error bars of the top and middle panels are one standard error in the spectra fitting. The error bars of the bottom panel are the combined uncertainty of energy and linewidth of exciton and umklapp features from the fitting (Supplementary Section 7). **d**, Reduced spin susceptibility as a function of electron density at different temperatures. Grey dashed lines are Curie susceptibilities in the Wigner crystal regime. Black dashed lines indicate the density $n_{WC}(T)$ at which the spin susceptibility deviates from Curie (left), the density $n_*(T)$ at which the slope changes (right) and the density n_{FL} above which the spin susceptibility does not exhibit temperature dependence. Inset: reduced spin susceptibility as a function of electron temperature at selected densities in the higher density regime. **e**, The product of reduced spin susceptibility and temperature as a function of electron density. The Curie susceptibility is depicted by a grey dashed line. At low densities, the data points at different temperatures align with the Curie susceptibility. The coloured dashed lines correspond to the linear interpolation of the susceptibility data between the density near $n_{WC}(T)$ and $n_*(T)$, obeying the lever rule. Deviations from the linear interpolation can be found in the vicinity of $n_{WC}(T)$ and $n_*(T)$ (see also Extended Data Fig. 5). The error bars in **d** and **e** are the combined fitting uncertainty of the slope of $\widetilde{M}(H)$ near zero density and one standard error of the zero-field slope of $\widetilde{M}(H)$.

finite spatial extent of crystalline correlations: the length scale can be estimated as $l_{corr}/a_{WC} \sim \Delta E_u/\delta E$, where l_{corr} is the correlation length representing the radius of the domain, a_{WC} is the lattice constant of the Wigner crystal and δE is the net contribution to the umklapp width from a finite correlation length. We obtained $l_{corr} \approx 3a_{WC}$ in the low-density regime ($n < n_{WC}$), indicating the presence of well-defined crystalline regions as in the previous report[22] (Supplementary Section 7). Between n_{WC} and n_*, l_{corr} decreases gradually and drops below a_{WC} at around n_*, indicating the continuous weakening of the crystalline correlations or a decrease in the size of the Wigner crystal domains.

In addition to the spectral anomalies and the umklapp feature, which provide insight into the evolution of the charge degree of freedom, we also extracted spin susceptibility from linear fits to $\widetilde{M}(H)$ curves measured using the single energy (1.636 eV) excitation, as described in the preceding section. In Fig. 3d, we show the evolution of the reduced spin susceptibility (χ/χ_0) as a function of electron density. We observed two abrupt changes in the slope of the spin susceptibilities near n_{WC} and n_*: below n_{WC}, the spin susceptibility follows a Curie law, $\chi \propto \frac{n}{T}$, as expected for independent spins localized to Wigner crystal lattice sites. Above n_*, the susceptibility decreased monotonically with density for all temperatures, which is consistent with a Fermi-liquid-like response (Fig. 3e). From this susceptibility data, we inferred the temperature evolution of the critical densities, $n_{WC}(T)$ and $n_*(T)$. Between $n_{WC}(T)$ and $n_*(T)$, the spin susceptibility showed an essentially linear dependence on density, with a slope different from the Curie susceptibility (Extended Data Fig. 5).

The data in Figs. 2 and 3 suggest two phase boundaries at $n_{WC}(T)$ and $n_*(T)$ that separate three phases: a Wigner crystal phase for $n < n_{WC}$, a liquid phase for $n > n_*$ and the intermediate phase occupying the range $n_{WC} < n < n_*$. The behaviour in the intermediate phase was consistent with a state in which only a fraction of the electrons participates in the formation of the crystal, with a lattice constant associated to the density n_{WC}. The persistence of exciton umklapp scattering implies that the size of the crystalline regions remains appreciable. The spin susceptibility in the intermediate phase is smaller than that expected for a Wigner crystal but, at low temperatures, is markedly enhanced relative to the high-density liquid. To first order, the susceptibility is well described by a linear interpolation between its values at n_{WC} and n_* (Fig. 3d,e). Taken together with the umklapp evolution, these observations indicate that the intermediate phase is a microemulsion phase with a nanoscale or mesoscale mixture of liquid and crystal regions, with the areal fractions of the two phases evolving with density according to the lever rule[1–3,7]. It is important to note that the intermediate phase is flanked by pronounced anomalies in a number of spectral observables (Fig. 1h,i and Extended Data Fig. 4), which suggests that it is a distinct thermodynamic phase rather than a broad crossover between the crystal and liquid.

Phase diagram and Pomeranchuk effect

The full temperature and density dependence of the data is summarized in the (n, T) phase diagram displayed in Fig. 4 (see Supplementary Section 8 for estimating electron temperature associated with n_{WC} and n_* from the reflectance measurement). The liquid region ($n > n_*(T)$) may be further divided into two distinct regions: Fig. 3d shows that although the spin susceptibility was essentially independent of temperature at the highest electron densities, it acquired a strong temperature dependence (Fig. 3d inset) below a characteristic density near 1.5×10^{12} cm^{-2}. We define the characteristic density $n_{FL}(T)$ as that at which the spin

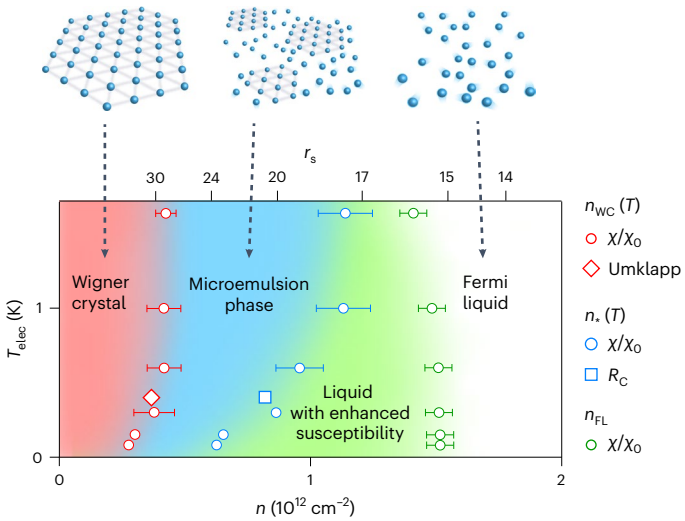

Fig. 4 | Phase diagram as a function of electron density and temperature. Phase boundaries are obtained by the following characteristic densities: $n_{WC}(T)$, $n_*(T)$ and n_{FL} from the spin susceptibility measurements (circles), $n_{WC}(T)$ from anomalies in umklapp scattering (diamond), and $n_*(T)$ from anomalies in reflectance spectra (square). The error bars associated with $n_{WC}(T)$ and $n_*(T)$ from the spin susceptibility measurements represent the density ranges that show deviations from the lever rule. The density n_{FL} is defined as that at which the spin susceptibility deviates from the highest temperature (3.28 K) spin susceptibility, and the error bars indicate the nearest data points from the deviation. See also Supplementary Fig. 18 for the phase diagram that includes the density-dependent Fermi temperature of the non-interacting 2DEG.

susceptibility deviates from the highest temperature (3.28 K) value. For densities $n_*(T) < n < n_{FL}(T)$, the spin susceptibility still increased with decreasing electron density but was, in general, larger than that expected for a conventional Fermi liquid. We note that near n_{FL} the exciton features evolved smoothly and there were no pronounced anomalies in the spin susceptibility, which suggests a crossover as opposed to a phase transition.

At temperatures below 1 K, both boundaries of the intermediate phase exhibited a rightward slant in the n–T phase diagram, which is indicative of the Pomeranchuk effect associated with enhanced stability of the crystalline phase upon heating due to its large spin entropy[1,7,33–36]. The overall magnitude of the effect was consistent with expectations based on QMC calculations[27] (Supplementary Section 9). The widening of the microemulsion phase upon increasing temperature also agreed qualitatively with theoretical predictions, although the width of the microemulsion phase is strongly underestimated. We found that n_* extended to higher densities at higher magnetic fields, which can be understood from the large Zeeman energy gain of the Wigner crystal from its enhanced spin susceptibility relative to the liquid (Extended Data Fig. 6).

Discussion and outlook

Our experiments demonstrate that the quantum melting of the Wigner crystal in a $MoSe_2$ monolayer proceeds by means of an intermediate microemulsion phase characterized by a nanoscale or mesoscale mixture of electron crystal and liquid. An important question is the extent to which quenched disorder, which is inevitably present in our sample, plays a role in the phenomenology we have reported. Strong disorder would imply substantial local variations within the sample. Our optical probe effectively averages over a spot with a diameter of around 1 μm; however, we observed sharp signatures of density-driven transitions, implying a negligible variation of critical densities across the measured area. Thus, the distinct character of electronic phases (liquid, crystal and microemulsion) that we observed was not compromised by disorder, as evidenced by the fact that the widths of the transitions were smaller than the width of the phase itself. On the Wigner crystal side, disorder may limit the crystalline correlations as evidenced by the finite umklapp width larger than the main exciton linewidth. Although not markedly altering the phases themselves, disorder may affect the competition between phases (for example, weak disorder is known to locally stabilize crystalline order[37]). In this context, a particularly striking observation is the large extent of the coexistence region, which is orders of magnitude larger than what clean limit theory predicts[38] (Supplementary Section 9). This discrepancy calls for more detailed studies of microscopic disorder effects.

Our results also reveal unconventional behaviour of the 2DEG in the liquid phase. In the density range $n_*(T) < n < n_{FL}(T)$, the spin susceptibility (Fig. 3d) has a much stronger temperature and density dependence than QMC[27] predictions. Weak disorder is also expected to result in an increase in susceptibility (logarithmic in $1/T$) in a Fermi liquid at low temperatures[39]. However, the pronounced increase that we observed in our data appears substantially stronger. In the same density range, the reflectance spectra also show some residual umklapp scattering with a linewidth that is considerably larger than in the proximate Wigner crystal and intermediate phases (Fig. 3a–c). Such behaviour may be due to local moments associated with residual crystallites. A more tantalizing possibility is a non-Fermi liquid regime driven by crystalline fluctuations near the onset of the inhomogeneous intermediate phase[40].

Our study serves as a starting point for investigating multiscale ordered phases of electronic matter, such as microemulsions of magnetic, superconducting and charge-ordered states[41–43]. The properties of such phases have been rarely studied and may harbour new functionalities, in particular, due to the prominent role of exotic interphase interfaces. The variety of correlated electronic phases observed recently in two-dimensional materials[24,44–46] provides a natural platform for further exploration of microemulsion phases by exploiting their facile tunability by means of, for example, multilayer heterostructures[23] or sample-gate distance[47,48]. Furthermore, local probes such as scanning tunnelling microscopy[45,49] or a scanning electron transistor[50] will enable the characterization and control of microemulsion phases at the nanoscale.

Online content

Any methods, additional references, Nature Portfolio reporting summaries, source data, extended data, supplementary information, acknowledgements, peer review information; details of author contributions and competing interests; and statements of data and code availability are available at https://doi.org/10.1038/s41567-024-02759-8.

References

1. Spivak, B. Phase separation in the two-dimensional electron liquid in MOSFET's. *Phys. Rev. B* **67**, 125205 (2003).
2. Spivak, B. & Kivelson, S. A. Phases intermediate between a two-dimensional electron liquid and Wigner crystal. *Phys. Rev. B* **70**, 155114 (2004).
3. Jamei, R., Kivelson, S. & Spivak, B. Universal aspects of Coulomb-frustrated phase separation. *Phys. Rev. Lett.* **94**, 056805 (2005).
4. Lorenzana, J., Castellani, C. & Castro, C. D. Phase separation frustrated by the long-range Coulomb interaction. I. Theory. *Phys. Rev. B* **64**, 235127 (2001).
5. Lorenzana, J., Castellani, C. & Di Castro, C. Phase separation frustrated by the long-range Coulomb interaction. II. *Phys. Rev. B* **64**, 235128 (2001).
6. Ortix, C., Lorenzana, J. & Di Castro, C. Frustrated phase separation in two-dimensional charged systems. *Phys. Rev. B* **73**, 245117 (2006).
7. Spivak, B. & Kivelson, S. A. Transport in two dimensional electronic micro-emulsions. *Ann. Phys.* **321**, 2071–2115 (2006).

8. Emery, V. J. & Kivelson, S. A. Frustrated electronic phase separation and high-temperature superconductors. *Physica C* **209**, 597–621 (1993).
9. Fäth, M. et al. Spatially inhomogeneous metal-insulator transition in doped manganites. *Science* **285**, 1540–1542 (1999).
10. Dagotto, E., Hotta, T. & Moreo, A. Colossal magnetoresistant materials: the key role of phase separation. *Phys. Rep.* **344**, 1–153 (2001).
11. Fogler, M. M., Butov, L. V. & Novoselov, K. S. High-temperature superfluidity with indirect excitons in van der Waals heterostructures. *Nat. Commun.* **5**, 4555 (2014).
12. Skinner, B. Chemical potential and compressibility of quantum Hall bilayer excitons. *Phys. Rev. B* **93**, 085436 (2016).
13. Wigner, E. On the interaction of electrons in metals. *Phys. Rev.* **46**, 1002–1011 (1934).
14. Drummond, N. D. & Needs, R. J. Phase diagram of the low-density two-dimensional homogeneous electron gas. *Phys. Rev. Lett.* **102**, 126402 (2009).
15. Kravchenko, S. V., Kravchenko, G. V., Furneaux, J. E., Pudalov, V. M. & D'Iorio, M. Possible metal-insulator transition at $B=0$ in two dimensions. *Phys. Rev. B* **50**, 8039–8042 (1994).
16. Yoon, J., Li, C. C., Shahar, D., Tsui, D. C. & Shayegan, M. Wigner crystallization and metal-insulator transition of two-dimensional holes in GaAs at $B=0$. *Phys. Rev. Lett.* **82**, 1744–1747 (1999).
17. Kravchenko, S. V. & Sarachik, M. P. Metal–insulator transition in two-dimensional electron systems. *Rep. Prog. Phys.* **67**, 1–44 (2004).
18. Shashkin, A. A. & Kravchenko, S. V. Recent developments in the field of the metal-insulator transition in two dimensions. *Appl. Sci.* **9**, 1169 (2019).
19. Hossain, M. S. et al. Anisotropic two-dimensional disordered Wigner solid. *Phys. Rev. Lett.* **129**, 036601 (2022).
20. Falson, J. et al. Competing correlated states around the zero-field Wigner crystallization transition of electrons in two dimensions. *Nat. Mater.* **21**, 311–316 (2022).
21. Ahn, S. & Das Sarma, S. Density-tuned effective metal-insulator transitions in two-dimensional semiconductor layers: Anderson localization or Wigner crystallization. *Physical Review B* **107**, 195435 (2023).
22. Smoleński, T. et al. Signatures of Wigner crystal of electrons in a monolayer semiconductor. *Nature* **595**, 53–57 (2021).
23. Zhou, Y. et al. Bilayer Wigner crystals in a transition metal dichalcogenide heterostructure. *Nature* **595**, 48–52 (2021).
24. Tang, Y. et al. Simulation of Hubbard model physics in WSe_2/WS_2 moiré superlattices. *Nature* **579**, 353–358 (2020).
25. Back, P. et al. Giant paramagnetism-induced valley polarization of electrons in charge-tunable monolayer $MoSe_2$. *Phys. Rev. Lett.* **118**, 237404 (2017).
26. Efimkin, D. K., Laird, E. K., Levinsen, J., Parish, M. M. & MacDonald, A. H. Electron-exciton interactions in the exciton-polaron problem. *Phys. Rev. B* **103**, 075417 (2021).
27. Attaccalite, C., Moroni, S., Gori-Giorgi, P. & Bachelet, G. B. Correlation energy and spin polarization in the 2D electron gas. *Phys. Rev. Lett.* **88**, 256601 (2002).
28. Knörzer, J. et al. Wigner crystals in two-dimensional transition-metal dichalcogenides: spin physics and readout. *Phys. Rev. B* **101**, 125101 (2020).
29. Yarlagadda, S. & Giuliani, G. F. Spin susceptibility in a two-dimensional electron gas. *Phys. Rev. B* **40**, 5432–5440 (1989).
30. Lifshitz, E. M. & Pitaevskii, L. P. *Statistical Physics: Theory of the Condensed State* (Elsevier Science, 2013).
31. Chakravarty, S., Kivelson, S., Nayak, C. & Voelker, K. Wigner glass, spin liquids and the metal-insulator transition. *Philos. Mag. B* **79**, 859–868 (1999).
32. Kim, K.-S., Murthy, C., Pandey, A. & Kivelson, S. A. Interstitial-induced ferromagnetism in a two-dimensional Wigner crystal. *Phys. Rev. Lett.* **129**, 227202 (2022).
33. Pomeranchuk, I. On the theory of liquid 3-He. *Zh. Eksp. Teor. Fiz.* **20**, 919–926 (1950).
34. Saito, Y. et al. Isospin Pomeranchuk effect in twisted bilayer graphene. *Nature* **592**, 220–224 (2021).
35. Rozen, A. et al. Entropic evidence for a Pomeranchuk effect in magic-angle graphene. *Nature* **592**, 214–219 (2021).
36. Clark, B. K., Casula, M. & Ceperley, D. M. Hexatic and mesoscopic phases in a 2D quantum Coulomb system. *Phys. Rev. Lett.* **103**, 055701 (2009).
37. Chui, S. T. & Tanatar, B. Impurity effect on the two-dimensional-electron fluid-solid transition in zero field. *Phys. Rev. Lett.* **74**, 458–461 (1995).
38. Joy, S. & Skinner, B. Upper bound on the window of density occupied by microemulsion phases in two-dimensional electron systems. *Phys. Rev. B* **108**, L241110 (2023).
39. Pudalov, V. M., Kuntsevich, A. Y., Gershenson, M. E., Burmistrov, I. S. & Reznikov, M. Probing spin susceptibility of a correlated two-dimensional electron system by transport and magnetization measurements. *Phys. Rev. B* **98**, 155109 (2018).
40. Oganesyan, V., Kivelson, S. A. & Fradkin, E. Quantum theory of a nematic Fermi fluid. *Phys. Rev. B* **64**, 195109 (2001).
41. Chowdhury, D., Orenstein, J., Sachdev, S. & Senthil, T. Phase transition beneath the superconducting dome in $BaFe_2(As_{1-x}P_x)_2$. *Phys. Rev. B* **92**, 081113 (2015).
42. Kagan, M. Y., Kugel, K. I. & Rakhmanov, A. L. Electronic phase separation: recent progress in the old problem. *Phys. Rep.* **916**, 1–105 (2021).
43. McGarrigle, E. C., Delaney, K. T., Balents, L. & Fredrickson, G. H. Emergence of a spin microemulsion in spin-orbit coupled Bose–Einstein condensates. *Phys. Rev. Lett.* **131**, 173403 (2023).
44. Regan, E. C. et al. Mott and generalized Wigner crystal states in WSe_2/WS_2 moiré superlattices. *Nature* **579**, 359–363 (2020).
45. Li, H. et al. Imaging two-dimensional generalized Wigner crystals. *Nature* **597**, 650–654 (2021).
46. Xu, Y. et al. Correlated insulating states at fractional fillings of moiré superlattices. *Nature* **587**, 214–218 (2020).
47. Skinner, B. & Shklovskii, B. I. Anomalously large capacitance of a plane capacitor with a two-dimensional electron gas. *Phys. Rev. B* **82**, 155111 (2010).
48. Li, T. et al. Charge-order-enhanced capacitance in semiconductor moiré superlattices. *Nat. Nanotechnol.* **16**, 1068–1072 (2021).
49. Xiang, Z. et al. Quantum melting of a disordered Wigner solid. Preprint at https://arxiv.org/abs/2402.05456 (2024).
50. Zondiner, U. et al. Cascade of phase transitions and Dirac revivals in magic-angle graphene. *Nature* **582**, 203–208 (2020).

Publisher's note Springer Nature remains neutral with regard to jurisdictional claims in published maps and institutional affiliations.

Springer Nature or its licensor (e.g. a society or other partner) holds exclusive rights to this article under a publishing agreement with the author(s) or other rightsholder(s); author self-archiving of the accepted manuscript version of this article is solely governed by the terms of such publishing agreement and applicable law.

© The Author(s), under exclusive licence to Springer Nature Limited 2025

Methods

Device fabrication and operation

Monolayer $MoSe_2$ and hBN flakes were exfoliated from bulk crystals onto 285 nm SiO_2/Si substrates. $MoSe_2$ monolayers were identified by an optical microscope. Thicknesses of hBN flakes in D1 were measured by atomic force microscopy to be 20 nm and 14 nm for the bottom and top layers, respectively. The flakes were stacked by the dry transfer method using a polydimethylsiloxane stamp and a thin layer of polycarbonate. The stacked heterostructure was then transferred onto the prepatterned bottom gate, which consisted of a 1 nm Cr layer and a 9 nm Pd–Au alloy layer fabricated using electron-beam lithography and thermal evaporation. Electrical contacts to the $MoSe_2$ layer and the bottom gate consisting of a 5 nm Cr layer and a 90 nm Au layer were deposited by means of thermal evaporation. For D2, hBN (53 nm), a $MoSe_2$ monolayer, hBN (50 nm) and a few-layer graphite (bottom gate) were picked up sequentially. The complete stack was placed on a SiO_2/Si substrate with prepatterned bottom metal, which consisted of a 1 nm Cr layer and a 9 nm Pt layer for the electrical contact to the $MoSe_2$ monolayer.

To dope the monolayer $MoSe_2$ at dilution refrigerator temperatures, we grounded the contacts to $MoSe_2$, applied a voltage V_{bg} to the back gate and at the same time illuminated the whole sample with a broadband light to activate the contacts. After doping was finished, the activation light was removed and the sample was thermalized for 0.5 s. The optical measurements were performed after the thermalization was finished. The doping onset voltage V_0 was determined as the voltage at which the reflectance contrast spectra or magneto-optical signal started to deviate from the neutral regime. The electron density was calculated from the parallel-plate capacitor model $n = \varepsilon_0\varepsilon_r(V_{bg} - V_0)/d_{bg}$, where ε_0 is the vacuum permittivity, $\varepsilon_r \approx 3.9$ is the dielectric constant of the hBN and d_{bg} is the thickness of the bottom hBN dielectric.

Optical measurements

Reflectance spectroscopy and magneto-optical measurements were performed with a home-built scanning confocal microscope based on a dilution refrigerator (Bluefors) with which the sample lattice temperature can reach 16 mK. The sample was mounted in the centre of a superconducting magnet (AMI) capable of applying ±9 T perpendicular magnetic field. A piezo-electric stage (attocube) was used to precisely position the sample. The microscope consisted of an apochromatic cryogenic objective (attocube LT-APO/LWD, numerical aperture 0.65), two fused silica plano-convex lenses (OptoSigma) at around 4 K and 50 K, two achromatic doublet lenses (Thorlabs) and a galvo scanner (Thorlabs). A compensated full-wave liquid crystal retarder (Thorlabs LCC1413-B) was placed in the shared light path of incoming and outcoming beams to impose the same $\pm\lambda/4$ retardance to both beams without mechanical movement. A polarimeter (Thorlabs PAX1000IR1) was used to confirm the circular polarization outside the dilution refrigerator. To ensure a polarization-independent light path inside the dilution refrigerator, we examined the reflection isotropy of a bare SiO_2/Si substrate mounted inside with a 360° rotation of the linearly polarized light.

For reflectance spectroscopy, a tungsten–halogen lamp (Thorlabs SLS201L) filtered to approximately 720–800 nm range was coupled to a single mode fibre, collimated with an objective (Olympus PLN ×10, numerical aperture 0.25) and directed to the sample, creating a diffraction-limited spot. The light power on the sample was variable but always kept below 0.7 nW. The reflected light was collected by a spectrometer with a 1,200 g mm^{-1} grating and a charge-coupled device camera (Princeton Instruments BLAZE). For magneto-optical measurements, we switched to a continuous-wave ultra-narrow linewidth Ti:sapphire laser (M Squared SOLSTIS) and limited light power on the sample to 60 fW (unless otherwise noted). The reflected laser was collected directly by a charge-coupled device camera (Princeton Instruments BLAZE).

Reflectance contrast spectroscopy

Reflectance contrast is defined as $R_C^*(E) = \frac{I(E)}{I_\infty(E)} - 1$, where $I(E)$ is the reflected light intensity and $I_\infty(E)$ is the reflected light intensity at an electron density that is high enough to bleach all excitonic resonances. In practice, we measured the reflected light intensity $I_{max}(E)$ at 1.0×10^{13} cm^{-2} and calculated $R_C(E) = \frac{I(E)}{I_{max}(E)} - 1$. At this density ($1.0 \times 10^{13}$ cm^{-2}), the exciton or RP resonance becomes negligible but some intensity from the AP still remains. Although fitting the exciton or RP resonance with a Lorentzian remains appropriate, fitting the AP resonance necessitates a removal of the residual background AP. To address this, we developed a procedure to subtract this background systematically. We note that $R_C(E) = \frac{I(E)}{I_{max}(E)} - 1 = \frac{I(E)/I_\infty(E)}{I_{max}(E)/I_\infty(E)} - 1 = \frac{R_C^*(E)+1}{R_{C\,max}^*(E)+1} - 1$. Because the reflectance contrast from the AP resonance at 1.0×10^{13} cm^{-2} is small $\left(R_{C\,max}^*(E) \ll 1\right)$, $R_C(E)$ can be approximated as, $R_C(E) \approx \left(1 + R_C^*(E)\right)(1 - R_{C\,max}^*(E)) - 1 = R_C^*(E) - \left(1 + R_C^*(E)\right)R_{C\,max}^*(E)$. Consequently, we obtained $R_{C\,max}^*(E) = \frac{1}{R_C^*(E)+1}\left(R_C^*(E) - R_C(E)\right)$.

To extract the exciton, RP and AP resonance parameters, we first fitted the exciton or RP resonance with a Lorentzian function $R_C^{X/RP}(n,E) = \frac{A^2}{(E-E_0)^2+\gamma^2/4}\left[\frac{\gamma}{2}\cos\alpha - (E-E_0)\sin\alpha\right] + C$, where A^2, E_0 and γ are the amplitude, energy and linewidth of the resonance. In the neutral regime ($n = 0$), there is only the exciton resonance, whereas at $n_{max} = 1.0 \times 10^{13}$ cm^{-2} the exciton or RP resonance is bleached. Therefore, $R_C^*(n = 0, E) \approx R_C^X(n = 0, E)$ and we could extract the density independent background contribution from the spectra at 1.0×10^{13} cm^{-2}: $R_{C\,max}^*(E) \approx R_C^X(n = 0, E) - R_C(n = 0, E)$. This background contribution was also fitted to a Lorentzian function. We then eliminated the fitted exciton and background Lorentzian function from each spectrum and fitted the rest, $R_C^{AP}(n,E) = R_C(n,E) - R_C^{RP}(n,E) + R_{C\,max}^*(E)$, with another Lorentzian function to extract the AP amplitude, energy and linewidth. Following the procedure of ref. 25, the onset density of the σ^- AP was then determined from a linear fitting to the σ^- AP amplitude as a function of density.

Magneto-optical measurements

Magneto-optical measurements using a single energy excitation were conducted at a fixed energy (1.636 eV) within a small magnetic field range of −1 T to 1 T. Because the bare exciton Zeeman splitting is small within this range of magnetic fields (≤0.1 meV for each $\sigma^\pm$ polarization), its contribution to the signal is small and can be subsequently subtracted. We also note that $I_{max}^{\sigma^+} \approx I_{max}^{\sigma^-}$ (reflection spectrum at a density of 1.0×10^{13} cm^{-2}) within −1 T to 1 T and $\widetilde{M} = \left(I^{\sigma^+}/I_{max}^{\sigma^+} - I^{\sigma^-}/I_{max}^{\sigma^-}\right)\left(I^{\sigma^+}/I_{max}^{\sigma^+} + I^{\sigma^-}/I_{max}^{\sigma^-}\right) \approx (I^{\sigma^+} - I^{\sigma^-})/(I^{\sigma^+} + I^{\sigma^-})$. We could thus use the reflected intensity instead of the normalized one to obtain $\widetilde{M}$. To convert the measured magneto-optical signal $\widetilde{M} = \frac{I^{\sigma^+} - I^{\sigma^-}}{I^{\sigma^+} + I^{\sigma^-}}$ to magnetization M, we introduced a density-dependent scaling factor, $A(n)$, that is field independent: $\widetilde{M} = A(n)M$. At high fields when the system is fully polarized, the magnetization is given by $M_S = \frac{1}{2}g\mu_B n$, so the scaling factor can be extracted using $A(n) = \frac{2\widetilde{M}_S}{g\mu_B n}$. Therefore, at an arbitrary field, the magnetization and susceptibility are $M = \frac{\widetilde{M}}{\widetilde{M}_S}\frac{1}{2}g\mu_B n$ and $\chi = \frac{d\widetilde{M}}{dH}\frac{1}{\widetilde{M}_S}\frac{1}{2}g\mu_B n$. The spin susceptibility of the non-interacting 2DEG is $\chi_0 = \left(\frac{g\mu_B}{2}\right)^2\frac{m^*}{\pi\hbar^2}$. Thus, the reduced spin susceptibility can be expressed as $\chi/\chi_0 = \frac{d\widetilde{M}}{dH}\frac{1}{\widetilde{M}_S}\frac{2\pi\hbar^2 n}{g\mu_B m^*}$. We used the conduction band g factor value of 4.3 (determined by fitting the measured $\widetilde{M}(n,H)$ using the Brillouin function at $n < n_{WC}$) and the effective mass of electrons, $m_e^* = 0.7m_0$.

Spin polarization from QMC data

To determine the theoretical evolution of the electronic spin polarization in an applied magnetic field H (Fig. 2a), we utilized existing QMC parametrizations of the ground state energy of the 2DEG as a function

of density (n) and polarization ζ. Ignoring orbital effects, which are small for the densities and magnetic field strengths under consideration, we wrote the energy per particle of the 2DEG in a magnetic field as $E(n,\zeta,H) = E(n,\zeta,H=0) - \frac{1}{2}g\mu_B\zeta H$, and we obtained the spin polarization by minimizing the energy: that is, $dE(n,\zeta,H)/d\zeta = 0$, which determined $\zeta(H)$. The function $E(n,\zeta,H=0)$ was previously parametrized by fitting to QMC simulations[27]. An example of this procedure is shown in Supplementary Section 10.

Data availability

Source data are provided with this paper. All other data are available from the corresponding authors upon reasonable request.

Acknowledgements

We acknowledge useful discussions with S. Kivelson, S. Das Sarma, A. Imamoglu, T. Smolenski, N. Leisgang and A. A. Zibrov. We thank T. Smolenski for sharing some of his unpublished data with us. We acknowledge support from AFOSR (FA9550-21-1-0216), the DoD Vannevar Bush Faculty Fellowship (N00014-16-1-2825 for H.P. and N00014-18-1-2877 for P.K.), NSF CUA (PHY-1125846 for H.P., E.D. and M.D.L.), Samsung Electronics (for H.P. and P.K.), NSF (PHY-1506284 for H.P. and M.D.L. and DGE-1745303 for E.B.), AFOSR MURI (FA9550-17-1-0002), ARL (W911NF1520067 for H.P. and M.D.L.) and DOE (DE-SC0020115 for H.P. and M.D.L. and DE-SC0022885 for Y.Z.). E.D. acknowledges support by the SNSF project no. 200021_212899. K.W. and T.T. acknowledge support from the JSPS KAKENHI (grant nos 19H05790, 20H00354 and 21H05233). The Flatiron Institute is a division of the Simons Foundation.

Author contributions

H.P. and E.D. conceived the project. J.S., J.W., G.S., Y.Z. and E.B. fabricated the samples and designed and performed the experiments. I.E. and P.A.V. performed calculations. I.E., P.A.V., Y.Y., M.A.M., S.Z., A.J.M. and E.D. contributed to theoretical descriptions. J.S., J.W., I.E. and P.A.V analysed the data. T.T. and K.W. provided hBN samples. J.S., J.W., I.E., P.A.V., E.D. and H.P. wrote the paper with extensive input from the other authors. H.P., E.D., P.K. and M.D.L. supervised the project.

Competing interests

The authors declare no competing interests.

Additional information

Extended data is available for this paper at https://doi.org/10.1038/s41567-024-02759-8.

Supplementary information The online version contains supplementary material available at https://doi.org/10.1038/s41567-024-02759-8.

Correspondence and requests for materials should be addressed to Eugene Demler or Hongkun Park.

Peer review information *Nature Physics* thanks the anonymous reviewers for their contribution to the peer review of this work.

Reprints and permissions information is available at www.nature.com/reprints.

https://doi.org/10.1038/s41567-024-02759-8

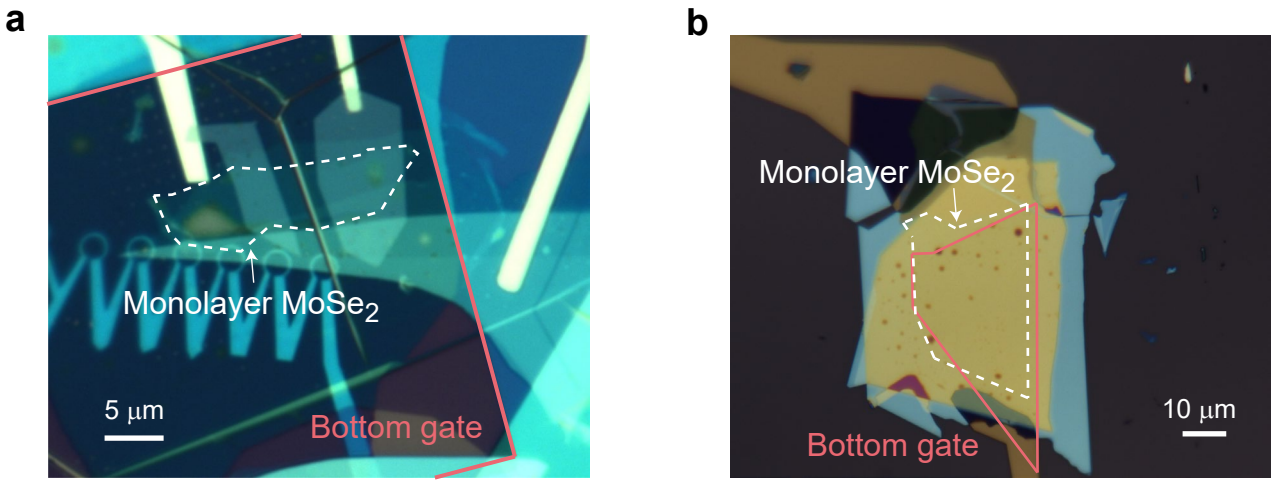

Extended Data Fig. 1 | Optical image of device 1 and device 2. a-b, Optical microscope image of (a) device **D1** and (b) device **D2**. The $MoSe_2$ monolayer regions are indicated by white dashed lines, and the solid red lines show the outline of the bottom gate electrode: (a) Pd/Au metal and (b) a few-layer graphite.

https://doi.org/10.1038/s41567-024-02759-8

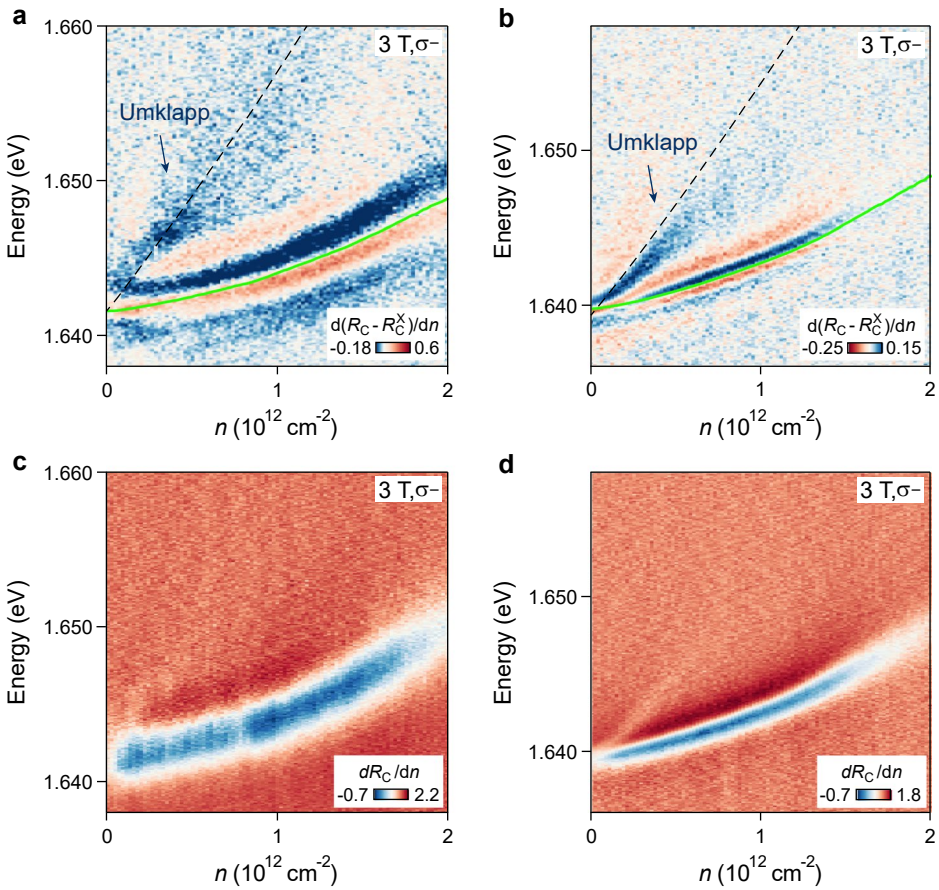

Extended Data Fig. 2 | Umklapp features in another spot in the original device, D1, and in another device, D2. Color map of the derivative of reflectance contrast spectra with respect to electron density at a base lattice temperature of 16 mK. A Lorentzian fitted exciton/RP peak was subtracted to emphasize the Umklapp features. The green line represents the fitted exciton/RP resonance energy, and the black dashed line indicates the expected resonance energy from umklapp scattering of excitons. Umklapp features in **D1** (another spot from that shown in main Fig. 1) and in another device, **D2**, are shown in **(a)** and **(b)**, respectively. Color map of the derivative of reflectance contrast spectra with respect to electron density, without subtracting the fitted exciton/RP Lorentzian in another spot in **D1 (c)** and in another device **D2 (d)**.

https://doi.org/10.1038/s41567-024-02759-8

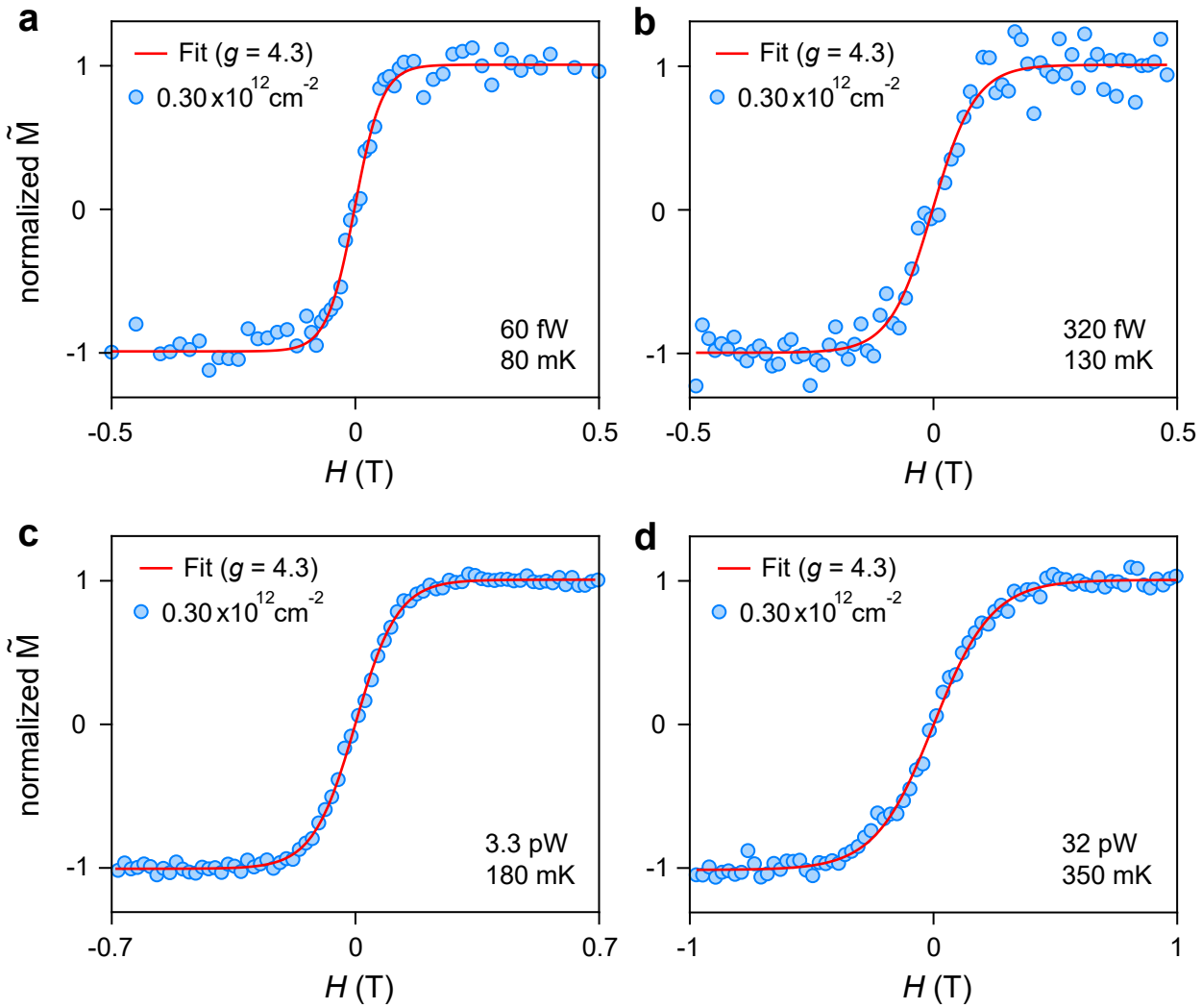

Extended Data Fig. 3 | Electron temperature estimation at low density under different incident light powers. a-d, We plot the signal $\widetilde{M}$ at the electron density of $0.30\times10^{12}\,cm^{-2}$ under varying light powers: **(a)** 60 fW, **(b)** 320 fW, **(c)** 3.3 pW, and **(d)** 32 pW. From a fit using the Brillouin function, we estimate the electron temperature. The estimated electron temperatures are: **(a)** 80 mK, **(b)** 130 mK, **(c)** 180 mK, and **(d)** 350 mK.

https://doi.org/10.1038/s41567-024-02759-8

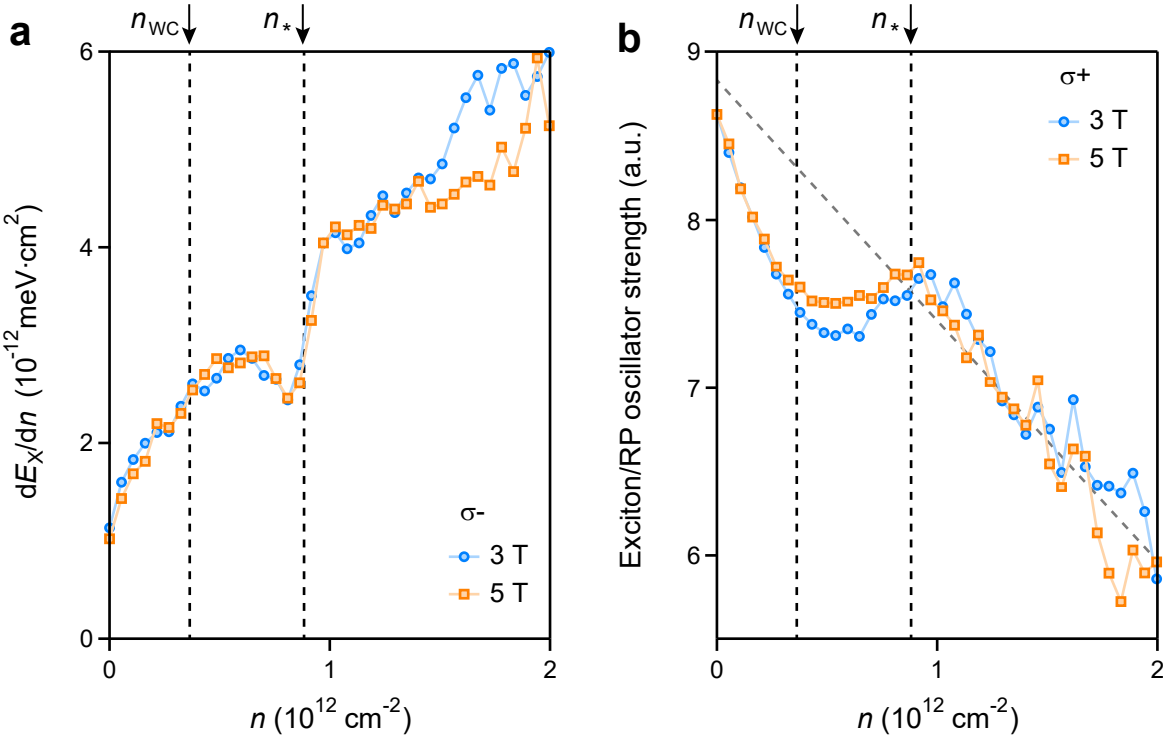

Extended Data Fig. 4 | Anomalies in the main excitonic properties. a, Near the density of $n_* = 0.9\times10^{12}$ cm^{-2}, a noticeable discontinuity in the derivative of the exciton/RP resonance energy with respect to electron density, dE_X/dn is observed, signifying a change in the slope of the exciton/RP resonance energy. **b**, A pronounced slope change of the oscillator strength is observed near the density of $n_* = 0.9\times10^{12}$ cm^{-2}. Reflectance contrast spectra measurements were performed under a light power of 0.7 nW at a base lattice temperature of 16 mK. The black arrows on the top x-axis and black dashed lines indicate the characteristic densities, n_{WC} and n_*. Linear decrease of the oscillator strength upon doping is represented by the grey dashed line. The measured excitonic properties are a convolution of the intrinsic properties of its electronic environment and the details of how the exciton couples to the electrons. In particular, the exciton is sensitive to the electronic compressibility. Non-analytic behavior of the compressibility at the microemulsion-liquid transition should therefore be expected to lead to rapid changes in the excitonic properties.

https://doi.org/10.1038/s41567-024-02759-8

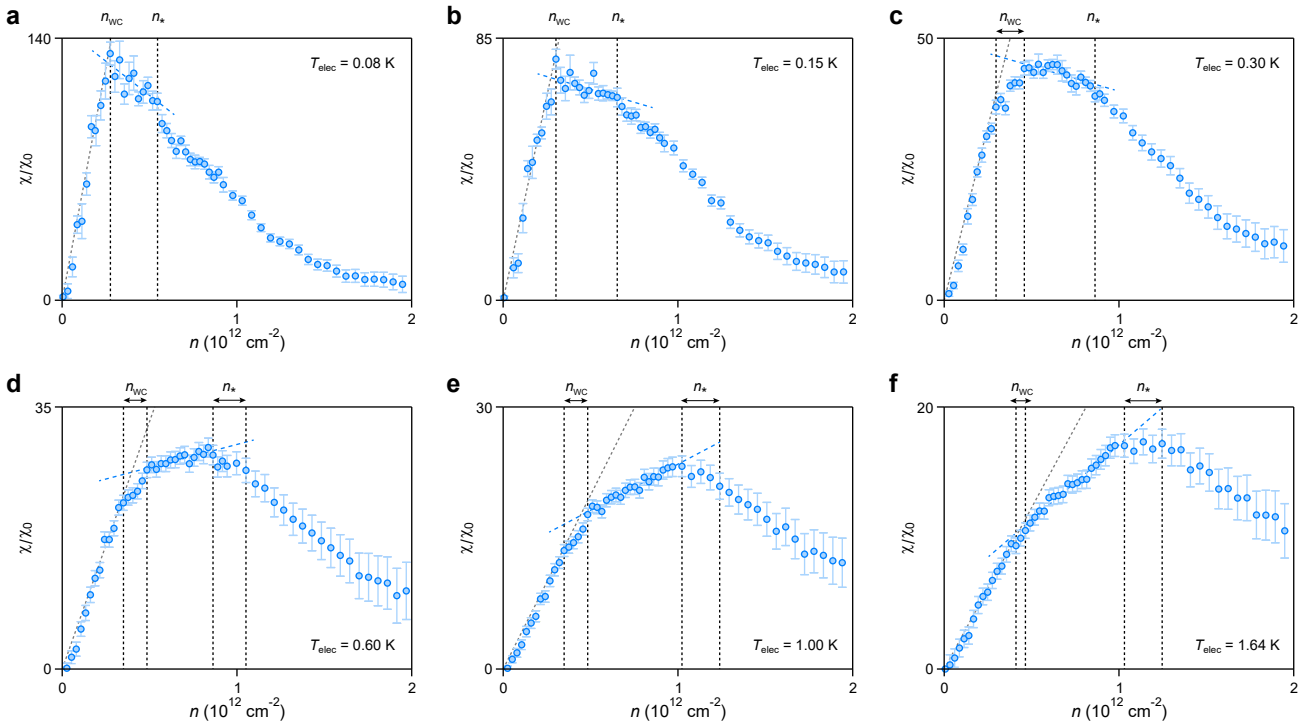

Extended Data Fig. 5 | Reduced spin susceptibility as a function of electron density at different temperatures. a-f, The Curie susceptibilities in the Wigner crystal regime are indicated by grey dashed lines. The spin susceptibility between n_{WC} and n_* aligns well with the colored dashed lines, representing intermediate density ranges that follow the lever rule. However, notable deviations from this linear behavior are observed in the vicinity of n_{WC} and n_*, signifying interface effects between the crystal and liquid regions. The boundaries of these density ranges are delineated by black vertical dashed lines, with these regions further emphasized by black arrows. The density ranges are quantified by the error bars in Fig. 4 of the main text. The determination of the transition near n_* and the density ranges are described in Fig. S19.

https://doi.org/10.1038/s41567-024-02759-8

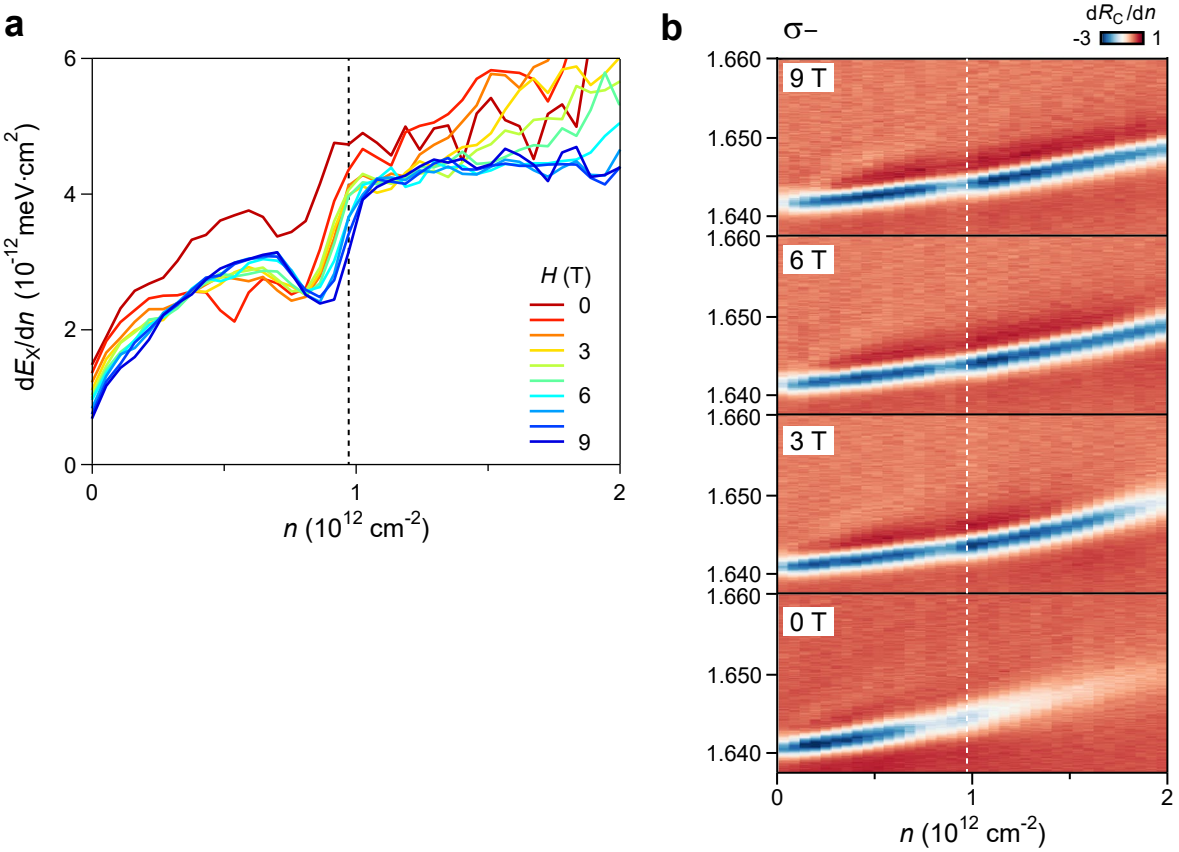

Extended Data Fig. 6 | Magnetic field dependence of n.. a, Derivative of fitted exciton/RP resonance energy with respect to electron density for left circularly polarized reflectance contrast at various magnetic fields. The black dotted line marks the electron density (n_*) that corresponds to the center of the jump in dE_X/dn at 9 T. **b**, Color maps showing left circularly polarized differential reflectance contrast are plotted as a function of electron density at various magnetic fields. The white dotted line marks the electron density at which the discontinuity (n_*) occurs at 9 T.